

Gravity wave breaking in two and three dimensions

2. Three-dimensional evolution and instability structure

David C. Fritts and Joseph R. Isler

Laboratory for Atmospheric and Space Physics and
Department of Electrical and Computer Engineering University of Colorado, Boulder

Øyvind Andreassen

Norwegian Defense Research Establishment, Kjeller

Abstract. A companion paper by Andreassen et al. (this issue) introduced and used a nonlinear, compressible, spectral collocation code to address the relative evolutions of two-dimensional motions obtained in two- and three-dimensional simulations of gravity wave breaking. That study illustrated the effects of instability on the wave field and mean flow evolution and suggested that two-dimensional models are unable to fully describe the physics of the wave breaking process. The present paper examines in detail the structure, evolution, and energetics of the three-dimensional motions accounting for wave instability as well as their associated transports of momentum and heat. It is found that this instability comprises counterrotating vortices which evolve very rapidly within the convectively unstable region of a breaking wave. Instability scales are selected based on wave geometry and vortices are elongated in the streamwise direction (horizontal wavenumber in the spanwise direction) and result in the rapid collapse of superadiabatic regions within the wave field. The resulting spectra show clearly the transition from gravity wave forcing of harmonics of the incident wave to instability onset and evolution. Fluxes of momentum and heat by the instability reveal the manner in which the gravity wave amplitude is constrained and the influences of instability on the wave transports of these quantities. The breakdown of the instability structure and its evolution toward isotropic small-scale structure is the subject of the companion paper by Isler et al. (this issue).

Introduction

In a companion paper by *Andreassen et al.* [this issue], we compared the influences of two- and three-dimensional (2-D and 3-D) instabilities on the evolution and amplitude of a gravity wave that became convectively unstable due to upward propagation in a density-stratified atmosphere. When motions were confined to the plane of wave propagation, instability took the form of spanwise-uniform rolls within regions of convective/shear instability that evolved relatively slowly, persisted for long times, and caused a systematic extraction of energy from the incident wave field. Because of the gradual evolution of these structures the incident wave field maintained amplitudes well in excess of those required for convective instability, yielding large vertical fluxes of wave energy and momentum.

Simulations that permitted 3-D instability structures, in contrast, exhibited a rapid instability growth, strong constraints on the incident wave amplitude, and much reduced vertical fluxes of wave energy and momentum in and above the region of wave breaking. As a consequence we concluded that 2-D simulations appear unable to capture the essential physics of the wave breaking process. The purpose of this paper is to describe in detail the structure, evolution, and energetics of the instability that accounts for wave saturation in the 3-D evolution.

We begin by displaying the effects of 3-D instability in the potential temperature field, both with time and height, in section 2. These illustrations emphasize the departures of the 3-D evolution from that occurring in 2-D and reveal the complexity of the motion field accompanying wave instability. The velocity and vorticity fields associated with the 3-D instability structure are discussed in section 3 and reveal that the instability comprises counterrotating vortices which evolve very rapidly due to convective instability within a breaking wave. Horizontal 2-D spectra are presented in section 4 and exhibit both the forcing of harmonics of the in-

Copyright 1994 by the American Geophysical Union.

Paper number 93JD03436.
0148-0227/94/93JD-03436\$05.00

cident wave with no transverse ($k_y \neq 0$) structure and the onset and evolution of instability at large transverse wavenumbers. The evolution and sources of instability energy are examined in section 5, while section 6 provides a discussion of the fluxes of momentum and heat by the instability structures. The conclusions of our study are presented in section 7.

Evolution of the Motion Field

Our 3-D gravity wave simulation was performed in stacked domains with dimensions $(4,2,4)H$ and $(4,2,1.5)H$, with the lower (larger depth) domain used for gravity wave excitation and the upper domain used to examine wave instability at higher (isotropic) resolution. Gravity wave propagation was in the x direction with an intrinsic frequency in the lower domain of $\omega = \pi\gamma N/10\sqrt{\gamma-1} \sim N/\sqrt{2}$, where N is the buoyancy frequency. A shear flow in the upper domain was imposed to confine wave instability to the interior of this domain and resulted in an intrinsic frequency at the breaking level of $\omega \sim N/10$. The wave motion was forced for ~ 3 wave periods as described by *Andreassen et al.* [this issue], and wave instability was seeded by addition of a 3-D noise spectrum and evolved following attainment of convective instability within the wave field after cessation of the wave forcing in the lower domain. The discussion in the remainder of this paper refers, for convenience, to quantities nondimensionalized by the density scale height H , the sound speed $c_s = \sqrt{\gamma g H}$, and a time scale H/c_s .

To illustrate the evolution of the motion field and the initial development of instability, we show in Plates 1 and 2 the temporal and spatial variations of the potential temperature field at the site of wave instability in a reference frame moving with the horizontal phase speed of the forced wave motion. Plate 1 displays the structure of a constant potential temperature surface at a height that intersects the site of primary instability within the wave field at $t = 62.5, 65, 67.5, 70, 72.5$, and 75 . Plate 2 illustrates the vertical structure of the motion field with surfaces of constant potential temperature spanning the instability at $t = 70$.

These figures reveal a 3-D and highly complex evolution of the wave field, with the primary, initially 2-D wave becoming increasingly distorted by an instability structure which appears to be aligned along the plane of wave propagation (a horizontal wavenumber in the spanwise direction). At several transverse locations the wave front appears to be buoyed up and retarded by the instability, while at intermediate locations the fluid is advanced and driven downward. Relative fluid motion beneath the upward displacements is opposite to that of wave propagation (wave propagation is toward the viewer and positive x), leading to long tongues of fluid extending rearward of the mean wave structure. Fluid that is advanced ahead of the mean wave structure by the instability is seen to splash back down and generate smaller-scale motions and additional structures elongated in the streamwise direction. Viewing these fields from below (not shown) also reveals long filaments

of high potential temperature fluid looping around the regions of splashing and extending to large distances behind the wave front. Finally, the wave front in the temporal evolution shown in Plate 1 is seen to remain at the same location with time because of our chosen reference frame. However, the small-scale structures excited by the nonlinear wave breaking process are seen to be advected rearward relative to the incident wave as they become decoupled from the primary wave motion (see the splashing structures at $t = 70$ to 75 in Plate 1).

Small-Scale Structures

We now consider the small-scale motions that account for the observed structure in the potential temperature surfaces in Plates 1 and 2. These motions are illustrated with eddy ($k_y \neq 0$) 3-D velocity vectors confined to vertical and horizontal planes intersecting the instability structure at the wave front at $t = 65$ in Plate 3. The vector field in the vertical plane reveals that each region where the wave front is buoyed up relative to the mean ($k_y = 0$) structure contains two counterrotating cells, with upward motions at the center and downward motions at the edges, corresponding closely to the displacements noted in the above discussion. There is, in addition, a two-cell structure in the vector field in the horizontal plane in each region which shows that there is motion (1) inward (toward negative x) beneath the wave front where the vertical motion is upward and (2) outward (toward positive x) where the vertical motion is downward.

These fields reveal an instability structure suggestive of the longitudinal rolls observed in sheared convection [*Busse and Clever*, 1979; *Clever and Busse*, 1992] and also exhibiting similarities to the counterrotating vortices observed to arise in the evolution of unstable shear flows in laboratory experiments [*Browand and Troutt*, 1980, 1985; *Breidenthal*, 1981; *Jimenez*, 1983; *Bernal and Roshko*, 1986; *Lasheras et al.*, 1986]. In sheared flows, streamwise vorticity appears to arise from the "translative instability" examined by *Pierrehumbert and Widnall* [1982] and depicted by *Lasheras et al.* [1986]. Subsequent theoretical and modeling studies by *Nagata and Busse* [1983], *Klassen and Peltier* [1985], and *Metcalfe et al.* [1987] appear to support these conclusions. Related efforts for a breaking wave environment by *Clark and Farley* [1984], *Winters and Riley* [1992], and *Winters and D'Asaro* [1993] have provided evidence of an instability structure with several similarities but also important differences.

To examine the instability structures more quantitatively, we present in Plate 4 the same evolution displayed in Plate 1 but with positive and negative contours of the x component of vorticity, $\zeta_x = \partial w/\partial y - \partial v/\partial z$, included to illustrate the development and effects of these structures. These images show the vortex pairs to evolve within and remain closely aligned with the convectively unstable portion of the wave field at early times in the instability evolution. As discussed above, each upward displacement of the wave front corresponds to a vortex pair, with upward motions at the

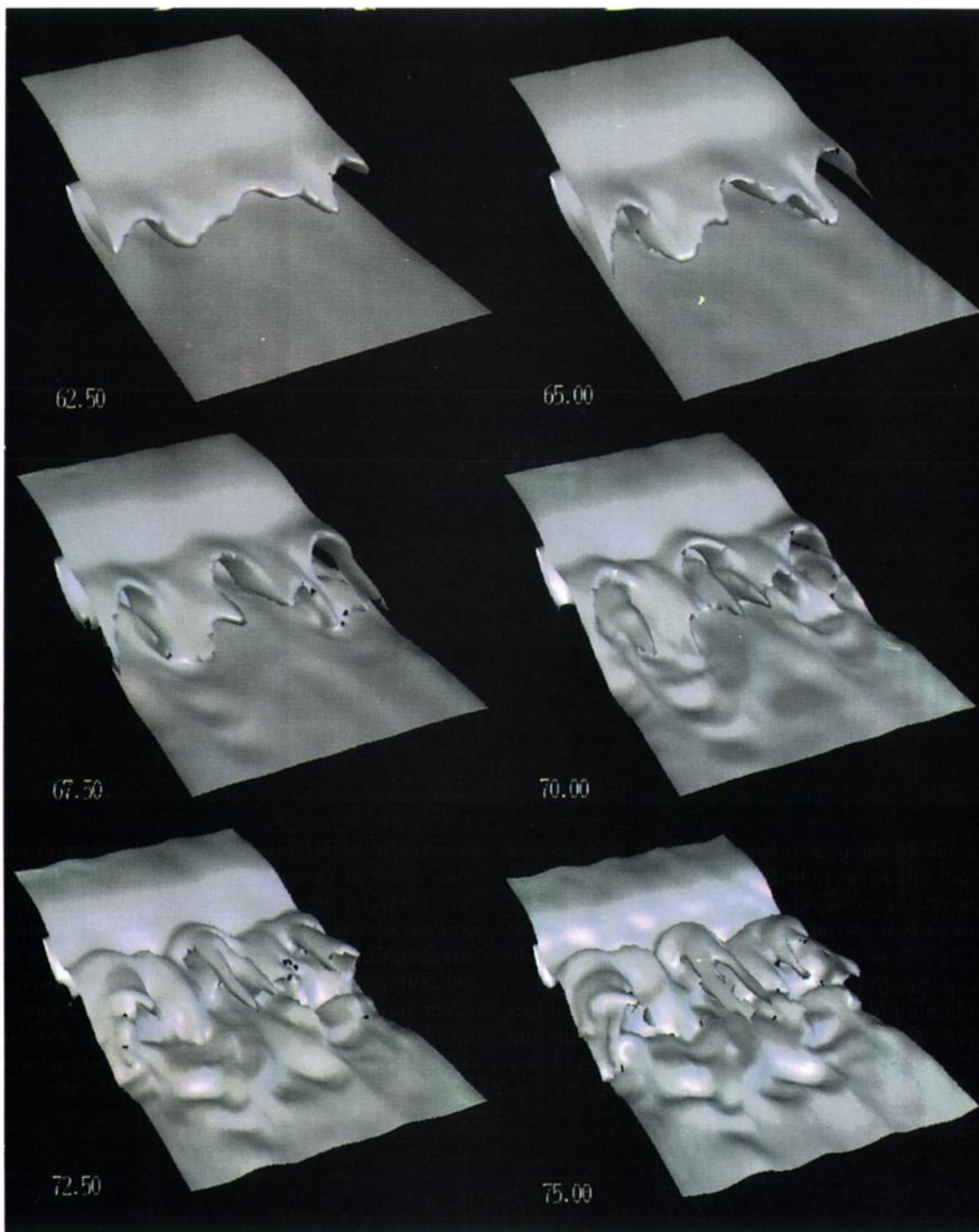


Plate 1. An isosurface of potential temperature within the region of primary wave breaking for the three-dimensional gravity wave simulation at the nondimensional times shown.

center and downward motions at the edges. Rearward motion of the fluid (toward negative x) beneath each vortex pair and forward motion between adjacent vortex pairs also implies advection of vorticity in a manner suggestive of the “translative instability” of *Pierrehumbert and Widnall* [1982] and the laboratory observations of shear flows cited above. Unlike the shear flow instability, however, the vortices are initiated along the phase of the wave motion where convective overturning first becomes significant. Thereafter, they intensify rapidly

and expand along the unstable phase of the wave until they occupy more than a full cycle of the motion field. There is, in particular, no evidence in our simulation that the streamwise vorticity arises due to undulation of initially spanwise vorticity.

The vortices occupy nearly the full depth of the unstable region and remain approximately circular throughout their early evolution, suggesting that their vertical and horizontal scales are dictated largely by the geometry of this region. At the early stages of instability,

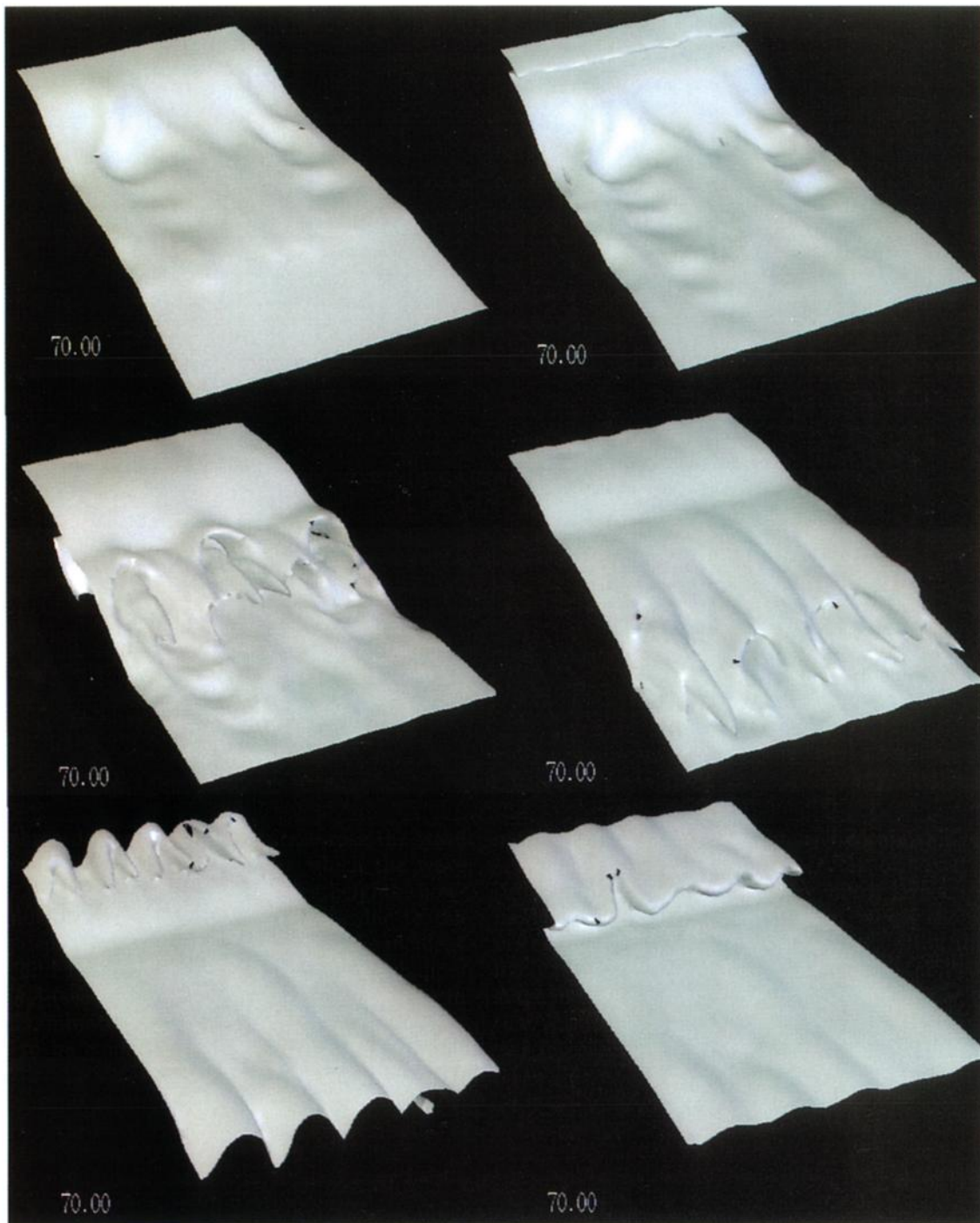


Plate 2. As in Plate 1 but for equally spaced surfaces spanning the region of wave instability at $t = 70$.

there are three dominant vortex pairs across the wave field because of the large depth over which the wave is unstable. At later times and greater heights, however, the number of vortex pairs increases due to the decreasing depth of the unstable portion of the incident wave field and the preferential growth of disturbances at larger $|k_y|$ (see the isosurfaces at greater heights in Plate 2). Examination of Plate 2 also reveals the vortex structures to be confined to the convectively unstable region within the wave field during early stages of the evolution, suggesting that their initial transports of mo-

mentum and heat occur primarily within this region.

Finally, the instability structures observed in this simulation occur at scales very much larger than the model resolution and the scale at which the spectral viscosity achieves nonzero values, suggesting that they likely represent the preferred mode of instability at this stage in the wave field evolution. Additionally, we note that a parallel simulation in which the noise variance was increased by 25 times yielded a virtually identical instability structure but which was advanced in time by $\Delta t \sim 5$ due to the more energetic excitation. Thus

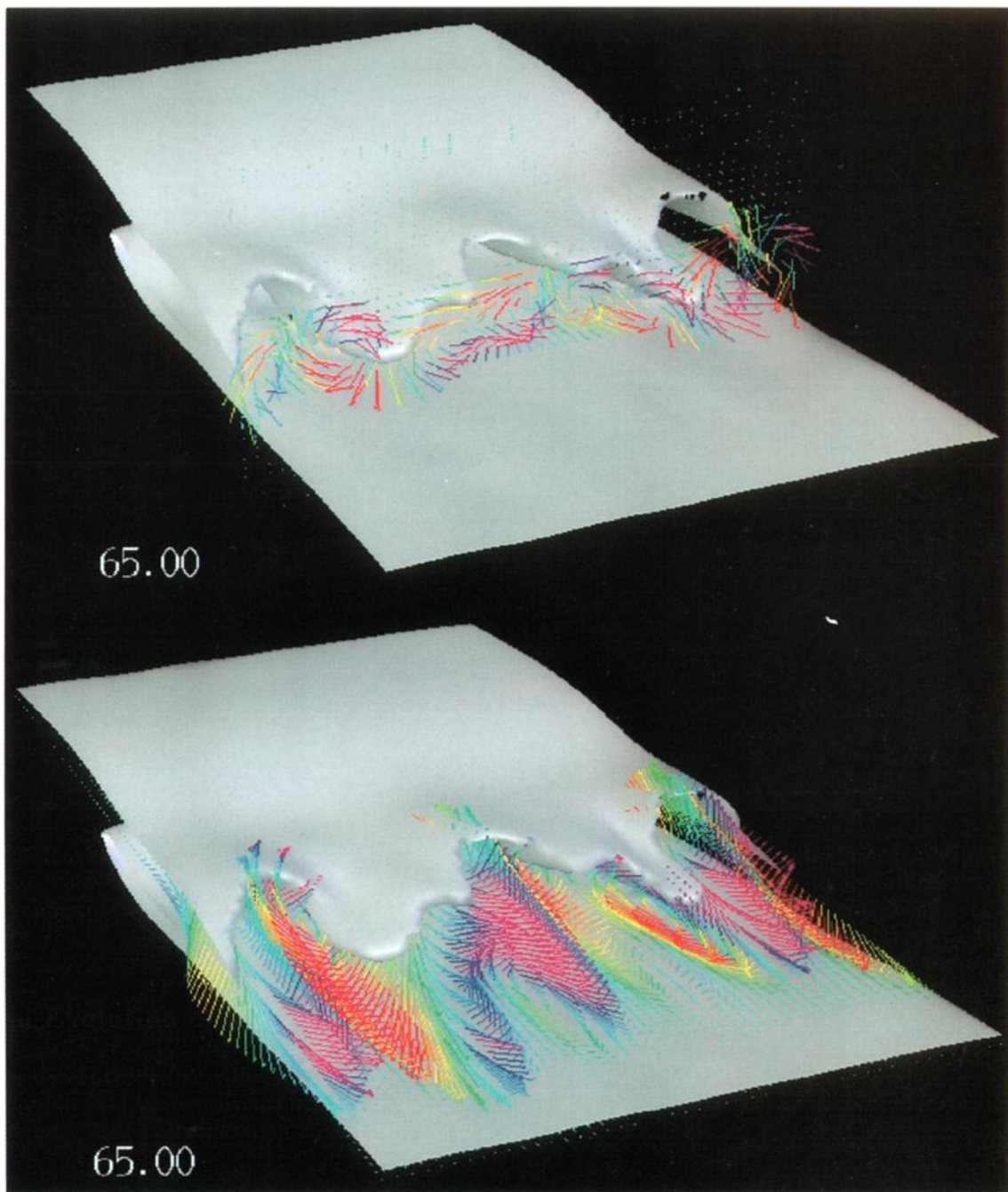


Plate 3. As in Plate 1 within the region of primary wave breaking with three-dimensional perturbation velocity vectors in (a) vertical (y, z) and (b) horizontal (x, y) planes at $t = 65$. Vectors are color coded by the magnitude of the transverse (y) component with maximum positive values maroon and maximum negative values red.

we are confident that the results presented here provide an accurate view of gravity wave breaking and instability at representative wave scales and high intrinsic frequencies.

Spectral Evolution of the Motion Field

We consider in this section the spectral character of the 3-D motion field to identify the scales of the dominant responses, their evolution with time and altitude,

and the distinctions between forced motions and instability structures. To do this, we first present one-dimensional (1-D) energy-content spectra ($kE(k)$) of kinetic energy in x and y as functions of time. We then show 2-D (k_x, k_y) spectra of the motion field to display more clearly the discontinuous nature of the energy transfer to instability scales.

One-Dimensional Spectra

The evolutions of the k_x spectrum for $k_y = 0$ and the k_y spectrum for $k_y \neq 0$ of kinetic energy, averaged

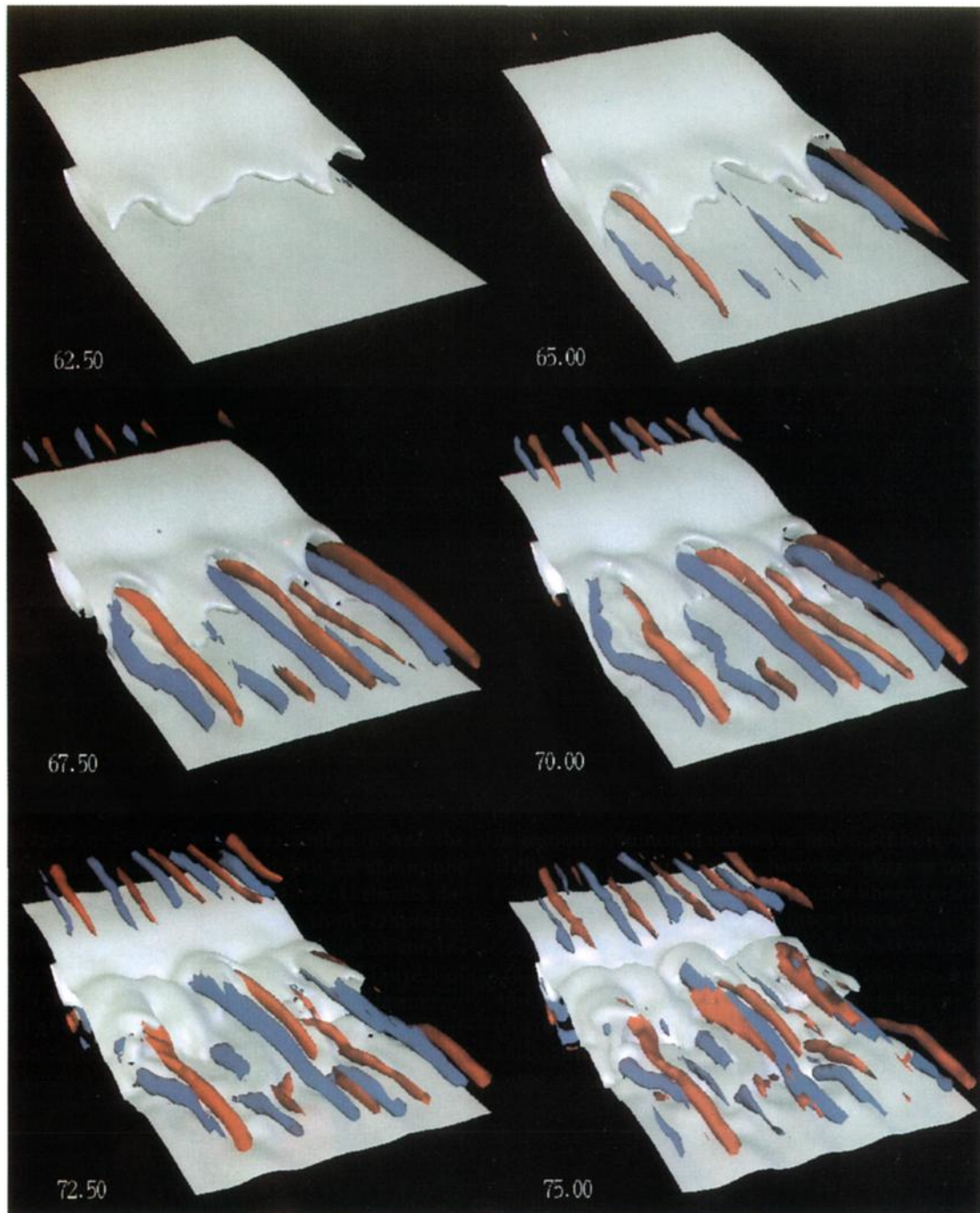


Plate 4. As in Plate 1 but including isosurfaces of zonal vorticity with blue positive and red negative for $|\zeta_x| = 2$.

over $0.2 \leq z_2/z_{2,0} \leq 0.6$, where z_2 and $z_{2,0}$ are the nondimensional height and domain depth for the upper domain, are shown in Figure 1. As in the 2-D results described by *Andreassen et al.* [this issue], the 1-D spectra exhibit an initial excitation of the harmonics of the incident gravity wave at $k_y = 0$ (compare with Figure 3 of that paper). Like the 2-D simulation, the kinetic energy is dominated at small $|k_x|$ by the horizontal component of the motion field; and as in the 2-D simulation, the 2-D ($k_y = 0$) structures in the 3-D simulation exhibit a systematic transfer of wave energy toward smaller scales

in response to nonlinear wave and instability processes. Unlike the 2-D simulation, however, there is only a weak tendency in the 3-D simulation for energies to increase at higher wavenumbers and later times.

In contrast to the k_x spectral evolution the k_y spectra display a discontinuous (in k_y) transfer of energy to and an explosive growth of energy at $|k_y| \sim 2\pi$ to 5π (corresponding to transverse wavenumbers 2 to 5) at early times in the instability evolution. These transfers occur prior to the excitation of motions at larger k_x and $k_y = 0$ in the 2-D evolution and are associated with the

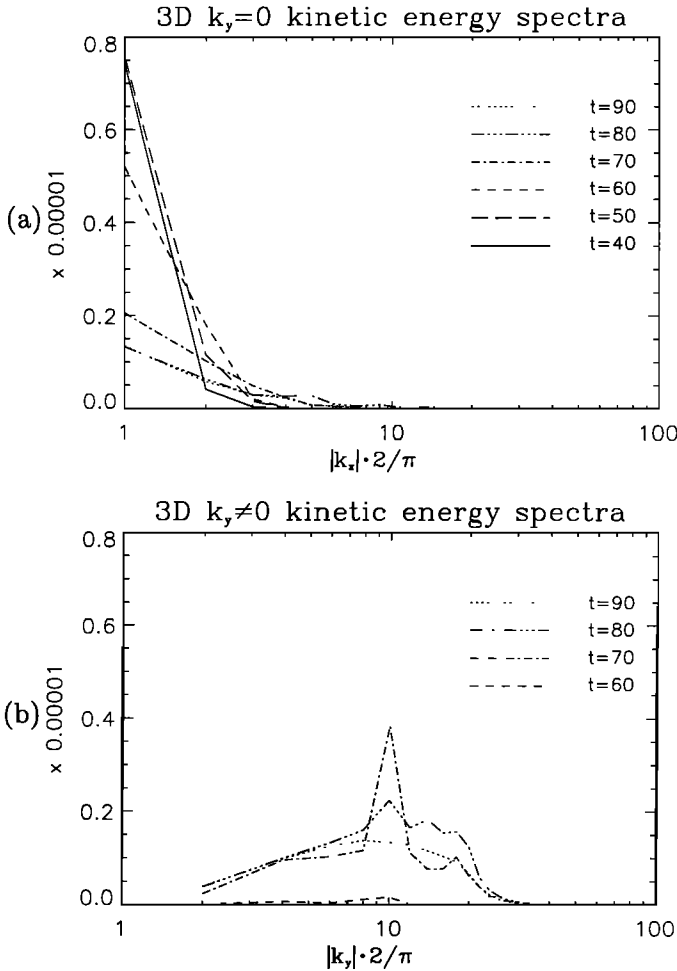


Figure 1. One-dimensional (a) k_x and (b) k_y energy-content spectra of kinetic energy at $t = 40, 50, 60, 70, 80,$ and 90 averaged over $0.2 < z_2/z_{2,0} < 0.6$.

3-D velocity fields and vortical structures seen to distort the potential temperature surfaces in Plates 1 to 4. At later times ($t > 70$), significant eddy kinetic energy occurs at wavenumbers extending from $|k_y| \sim 2\pi$ to 10π (transverse wavenumbers of 2 to 10) due to vortex breakdown and the continuing evolution toward smaller scales of motion. The decay of energy at larger wavenumbers is due to our spectral viscosity scheme included to avoid aliasing near the Nyquist wavenumbers.

The instability growth in the 3-D simulation is seen to limit the incident wave amplitude much more severely than in the 2-D simulation, as noted in the discussion of the 2-D and 3-D $k_y = 0$ results by *Andreassen et al.* [this issue]. Not seen in Figure 1, but apparent from the vorticity contours displayed in Plate 4, is the occurrence of the predominant kinetic energy of the instability at small $|k_x|$ because of their elongated streamwise and gradually sloping structure in this direction. This feature of the instability structure is revealed more clearly in the discussion of 2-D spectra below.

Two-Dimensional Spectra

The spectral evolution of the wave and instability field is displayed during the early stages of instability

growth and wave breakdown with 2-D (k_x, k_y) spectra of kinetic energy averaged over the same heights as above in Figure 2 at $t = 60, 65, 70,$ and 75 . The wavenumbers in each direction are nondimensional, and the common Nyquist wavenumbers in k_x and k_y are indicative of equal model resolution in each direction. These spectra show the initial expansion of wave energy from the incident motion at $k_x = \pm\pi/2$ (wavenumber 1) to larger $|k_x|$ and $k_y = 0$. Emergence of the vortex structures following the onset of instability then results in a discontinuous (in k_y) transfer of energy from the $k_y = 0$ structures to the instability scales at intermediate $|k_y|$. The spectral description of the subsequent instability evolution and the transition to smaller, more isotropic scales is presented in the companion paper by *Isler et al.* [this issue].

Another view of the wave and instability evolution is provided by 2-D (k_y, k_z) spectra of kinetic energy shown in Figure 3 at the same times as above and averaged over all x . Note, however, that the k_z spectra are expressed in terms of Chebyshev polynomials rather than Fourier harmonics and thus do not represent a unique relationship to different scales of motion. At early times, spectral energy is confined to the smaller $|k_z|$ at $k_y = 0$. But as the instability structures develop, there is again a transfer of energy from the $k_y = 0$ motions discontinuously to $|k_y| \sim |k_z| \sim 2\pi$ to 5π (wavenumbers of ~ 2 to 5). As the simulation progresses, the distribution of energy remains approximately isotropic in k_y and k_z but expands to larger ($|k_y|, |k_z|$) in response to the smaller unstable layer depths observed to evolve at later stages of the wave field evolution.

Instability Energetics

The energetics of the instability structures are examined by evaluating the kinetic energy of the eddy field ($k_y \neq 0$) and the different terms that contribute to eddy kinetic energy production and loss. To form an eddy kinetic energy equation, we must first separate the mean, 2-D wave, and 3-D eddy structures. This is done by writing the total velocity, density, and pressure fields as the sum of three terms,

$$\phi(x, y, z, t) = \bar{\phi}(z, t) + \tilde{\phi}(x, z, t) + \phi'(x, y, z, t), \quad (1)$$

where

$$\bar{\phi}(z, t) = \frac{1}{x_0 y_0} \int_0^{x_0} \int_0^{y_0} \phi(x, y, z, t) dx dy \quad (2)$$

$$\tilde{\phi}(x, z, t) = \frac{1}{y_0} \int_0^{y_0} \phi(x, y, z, t) dy - \bar{\phi}(z, t). \quad (3)$$

Products of perturbation quantities averaged in y are denoted

$$\langle \phi'_1 \phi'_2 \rangle(x, z, t) = \frac{1}{y_0} \int_0^{y_0} \phi'_1(x, y, z, t) \phi'_2(x, y, z, t) dy \quad (4)$$

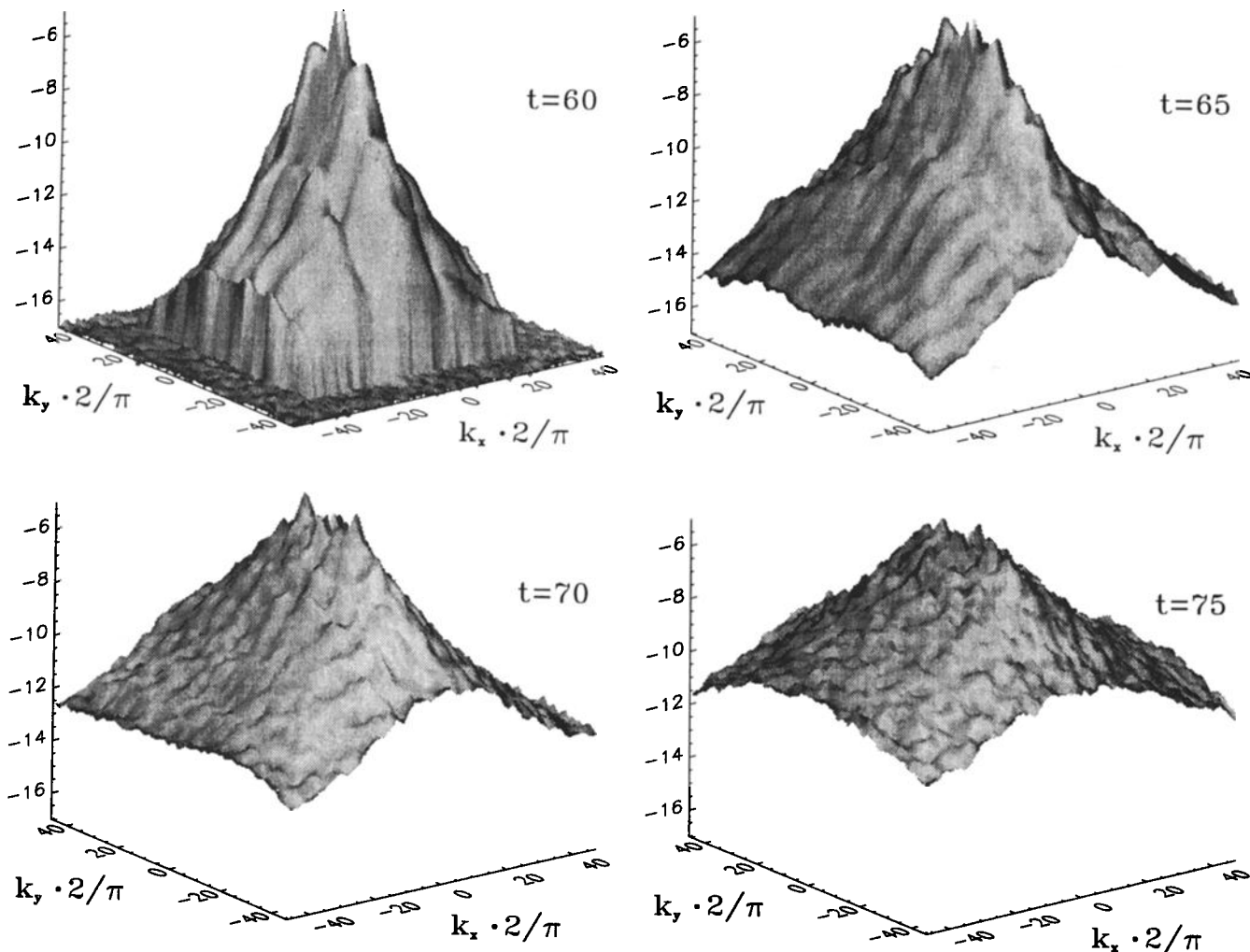


Figure 2. Two-dimensional (k_x, k_y) spectra of kinetic energy at $t = 60, 65, 70,$ and 75 averaged over $0.2 < z_2/z_{2,0} < 0.6$ showing the initial transfer of energy to larger $|k_x|$ at $k_y = 0$ and subsequently to intermediate $|k_y|$ at small $|k_x|$.

to distinguish them from the wave quantities, $\tilde{\phi}$, with $k_y = 0$.

Eddy Kinetic Energy Equation

With the above definitions, the nondimensional eddy kinetic energy averaged in y may be written

$$\langle E' \rangle = \frac{1}{2y_0} \int_0^{y_0} \rho u_i'^2 dy = \frac{1}{2} (\bar{\rho} + \tilde{\rho}) \langle u_i'^2 \rangle \quad (5)$$

where summation over repeated indices is assumed and we have neglected triple correlations of eddy quantities. For reference the corresponding expressions for nondimensional eddy potential and internal (or elastic) energies are

$$\langle P' \rangle = \frac{1}{2y_0} \int_0^{y_0} \frac{\rho}{\gamma - 1} \left(\frac{\theta'}{\theta} \right)^2 dy = \frac{1}{2} \frac{\bar{\rho} + \tilde{\rho}}{\gamma - 1} \frac{\langle \theta'^2 \rangle}{(\bar{\theta} + \tilde{\theta})^2} \quad (6)$$

$$\langle I' \rangle = \frac{1}{2y_0} \int_0^{y_0} \frac{\rho}{\gamma^2} \left(\frac{p'}{p} \right)^2 dy = \frac{1}{2} \frac{\bar{\rho} + \tilde{\rho}}{\gamma^2} \frac{\langle p'^2 \rangle}{(\bar{p} + \tilde{p})^2} \quad (7)$$

An equation describing the rate of change of the eddy kinetic energy is then obtained from equations (1) of *Andreassen et al.* [this issue] and given by

$$\begin{aligned} & \frac{\partial}{\partial t} \langle E' \rangle + (\bar{\mathbf{u}} + \tilde{\mathbf{u}}) \cdot \nabla \langle E' \rangle + \frac{\partial}{\partial x} \langle p' u' \rangle + \frac{\partial}{\partial z} \langle p' w' \rangle \\ &= -(\bar{\rho} + \tilde{\rho}) \langle u' u'_i \rangle \frac{\partial}{\partial x} \tilde{u}_i - (\bar{\rho} + \tilde{\rho}) \langle w' u'_i \rangle \frac{\partial}{\partial z} (\tilde{u}_i + \tilde{u}_i) \\ & \quad + \langle p' \nabla \cdot \mathbf{u}' \rangle - \langle \rho' w' \rangle g - \text{dissipation terms,} \end{aligned} \quad (8)$$

with the same assumptions as above.

The terms on the left-hand side of equation (8) are the local rate of change and advective change of $\langle E' \rangle$ and the energy flux (or pressure work) contributions. The terms on the right-hand side of equation (8) include the source/sink terms due to mean and wave wind shear, a pressure-source term expressing conversion between eddy kinetic and internal energies, a buoyancy term representing conversion between eddy kinetic and potential energies [Gill, 1982; Pedlosky, 1987], and the spectral viscosity described by *Andreassen et al.* [1993].

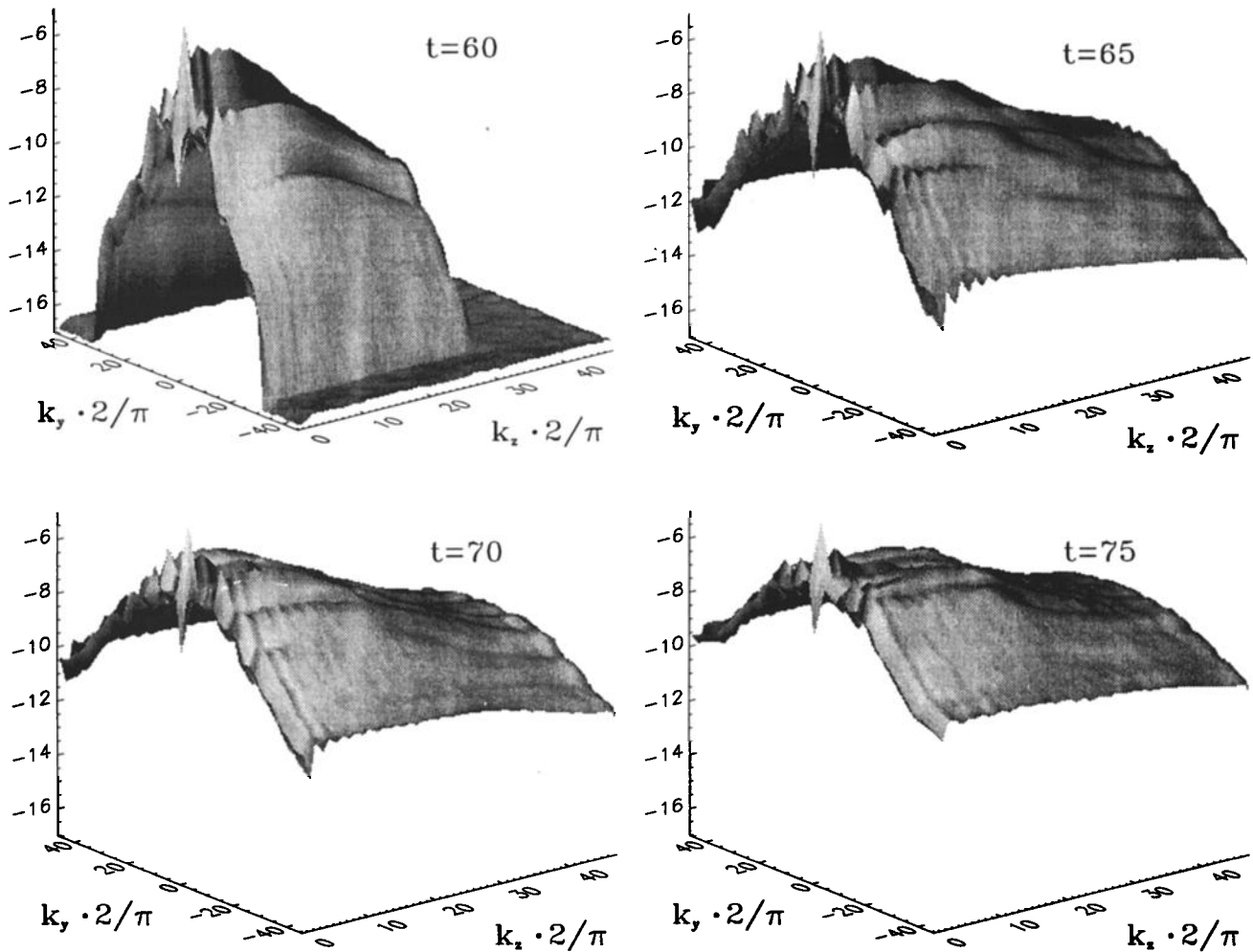


Figure 3. As in Figure 2, but for the two-dimensional (k_y, k_z) spectra showing the energy transfers to smaller scales in y and z . The spectra here are averaged in x .

Evolution of Eddy Kinetic Energy

The evolutions of the domain-averaged eddy kinetic energy in the 2-D and 3-D simulations were presented in Plate 1 and Figure 7 of *Andreassen et al.* [this issue]. There it was shown that the 3-D instability evolved much more rapidly and was significantly more effective at limiting the incident gravity wave amplitude than was the 2-D instability. Our intent here is to look at this eddy kinetic energy evolution in the 3-D simulation in greater detail by considering both its growth within the unstable regions and its decay once these vortex structures have been advected into the stable portion of the motion field. We consider only the evolution and energetics of the coherent vortex structures in this paper, however. Their subsequent evolution and breakdown to isotropic, small-scale structures is addressed in the companion paper by *Isler et al.* [this issue].

The distribution of eddy kinetic energy within the gravity wave field is shown at $t = 60, 65, 70,$ and 75 in Figure 4. Comparison of these distributions with the 2-D potential temperature profiles presented by *Andreassen et al.* [this issue] and reference to Plate 4 of this

paper show the eddy kinetic energy to be generated and initially confined within the convectively unstable portion of the gravity wave field, consistent with the 3-D mountain wave study by *Clark and Farley* [1984]. Vortex structures continue to develop and elongate within the unstable portion of the wave field as this extends through the wave at a constant phase, due to continued vertical propagation and compression of vertical scales. The vortices (and eddy kinetic energy) fail to propagate with the incident wave motion, however, and instead are advected with the local fluid motion into the stably stratified portion of the wave field where their growth ceases. This allows new vortices to form within the unstable regions, leading to vortex structures that are stacked in the vertical direction and eventually occupy the entire region of wave breaking (see the late-time evolution addressed in the companion paper by *Isler et al.* [this issue]). Because of the rapid growth of eddy kinetic energy within the unstable regions, however, maximum values remain closely aligned with the sites of convective or dynamical instability.

The advection of energetic vortex structures out of the region of convective instability, and the dynamical

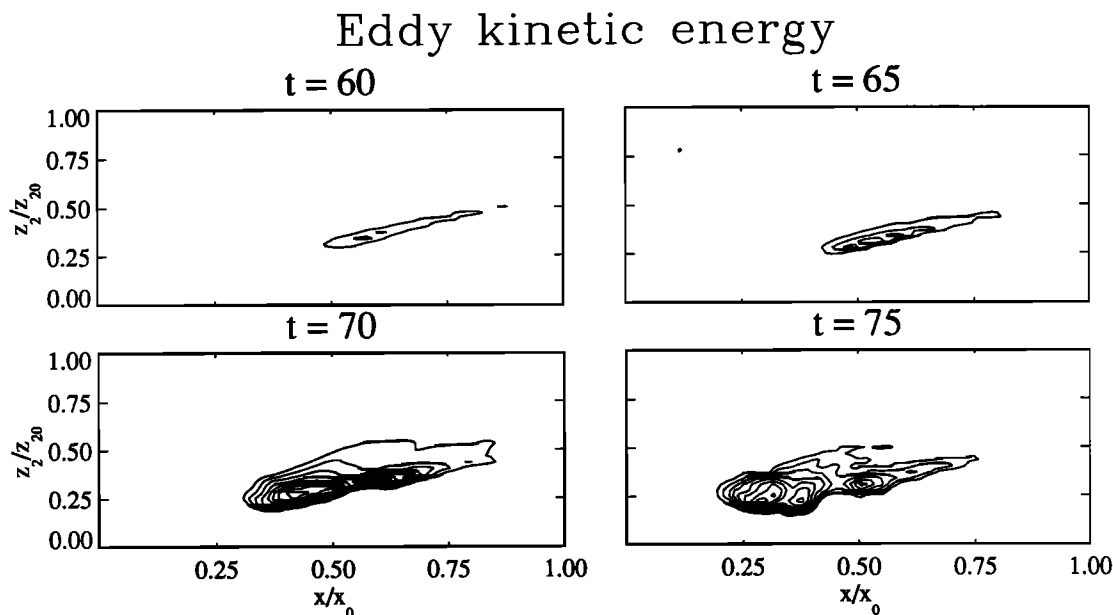


Figure 4. Cross sections in the (x, z) plane of eddy kinetic energy $\langle E' \rangle$ at $t = 60, 65, 70,$ and 75 . Contour intervals are 5×10^{-6} (zero not shown), with those at $t = 60$ smaller by a factor of 5. The maximum eddy kinetic energies occur at late times following wave collapse and shear instability.

instability at lower levels and later times, have important implications for mixing and transport processes in the atmosphere. The breakdown of these vortex and instability structures and their transition to isotropic turbulence is addressed by *Islar et al.* [this issue]. That study suggests that the induced turbulence will lead to significant vertical transports due to wave breaking, with implications for the relative efficiency of turbulent mixing of momentum and heat [*Fritts and Dunkerton, 1985; Coy and Fritts, 1988; McIntyre, 1989*]. We expect, however, that this mixing efficiency will also depend on the incident wave structure and the relative evolutions of eddy structures within and outside of convectively unstable layers. Thus an assessment of this mixing and the implied turbulent Prandtl number based on our model results will be deferred until we have performed simulations to longer times and for other wave breaking geometries.

Sources of Eddy Kinetic Energy

We anticipate, on the basis of the stability analysis by *Winters and Riley [1992]* and studies of longitudinal rolls in Rayleigh-Benard convection, that a major source of eddy kinetic energy will be the buoyancy term because the streamwise rolls are a manifestation of a convective instability of the incident gravity wave motion. Nevertheless, the large shears present in the mean and gravity wave motion fields may also contribute to the creation of eddy structures, while the pressure-source term cannot be discounted without evaluation because it represents a conversion from eddy internal to eddy kinetic energy.

To assess these various eddy kinetic energy sources and sinks, we evaluate each term locally and averaged throughout the upper domain. The domain-averaged values are shown as functions of time in Figure 5 and reveal that the buoyancy term is indeed a major source of eddy kinetic energy prior to $t \approx 70$. Wave and mean shear terms also contribute to the generation of eddy kinetic energy of the vortex structures due to the strong shears occurring at the lower edge of the convectively unstable region at $t \sim 60$ to 70 . After the initial wave collapse ($t > 70$), however, the dominant source of eddy

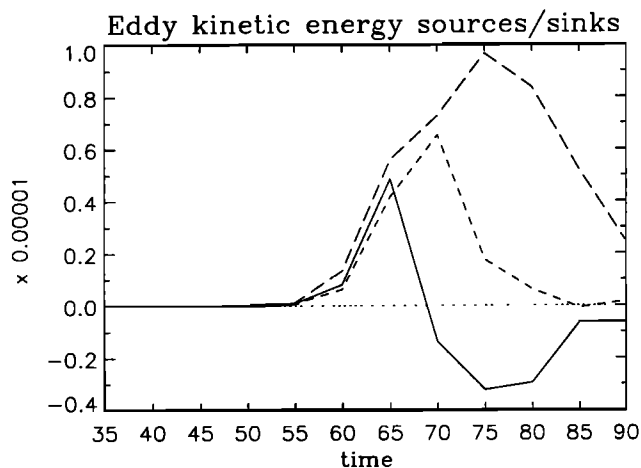


Figure 5. Eddy kinetic energy source/sink terms averaged throughout the upper domain as functions of time. The three curves show the buoyancy (solid), vertical shear (long dashed), and horizontal shear (short dashed), respectively.

kinetic energy is the strong vertical shear of the horizontal motion field at lower levels associated with very small local Richardson numbers in this region (see the discussion of this feature by *Isher et al.* [this issue]). The major contributor to each shear term is the zonal (x) component because of the dominance of wave variance by \bar{u} and of eddy variance by u' . Relative to the buoyancy and shear terms, the pressure-work terms contribute very little to the creation or destruction of eddy kinetic energy because they represent boundary effects, while the eddy structures have evolved apart from such influences. Likewise, the pressure-source term is small because of the very small magnitude of the eddy internal energy available for conversion (see below).

Contours of the buoyancy, vertical shear, and horizontal shear source/sink terms in the (x, z) plane are shown at $t = 60, 65, 70,$ and 75 in Figures 6 to 8. Note that the contour intervals are the same for each figure, but are smaller by a factor of 5 at $t = 60$ in order to display the structure with similar resolution at each time. Figure 6 shows the buoyancy term to lead to eddy kinetic energy creation within the convectively unstable regions at early times and to its destruction within the stably stratified fluid outside these regions at later times, as suggested by the domain-averaged results in Figure 5. In contrast, the vertical and horizontal shear terms act as both sources and sinks of eddy kinetic energy at early times but contribute preferentially to generation due to the large shears at lower levels. The effects of the shear terms for $t \geq 70$ are partially offsetting, with corresponding (but opposite) source and sink regions, but with the source terms larger in magnitude reflecting the net generation of eddy kinetic energy by the strong wave and mean shears at lower levels and later times.

Evolution of Wave and Eddy Kinetic, Potential, and Internal Energies

Vertical profiles of kinetic, potential, and internal energy for the 2-D ($k_y = 0$) and 3-D ($k_y \neq 0$) wave and eddy structures are displayed at $t = 50, 60, 70, 80,$ and 90 in Figure 9. These profiles reveal the energy in the 2-D fields to be approximately equipartitioned between kinetic and potential, with some oscillation between the two components in both space and time, due to wave superposition. At early times the major contribution is due to the incident wave as it evolves in the strong mean shear at lower levels. As energy is transferred to harmonics of this wave structure, however, the incident wave energy decays and the primary contribution at later times occurs in response to the strong shears and dynamical instability induced by the incident wave momentum transports at earlier times (see Figures 8 and 9 of *Andreassen et al.* [this issue]). The internal energy within the 2-D motion field, by contrast, is smaller by a factor of ~ 100 and clearly makes almost no contribution to the overall wave field energetics.

Energy in the 3-D motion field arises initially in the potential energy component in two distinct height intervals (see Figure 9). This component achieves a maximum at $t \sim 60$ and spreads vertically throughout the region of wave instability thereafter. The eddy kinetic energy, in contrast, is initially much smaller than the eddy potential energy but surpasses it at $t \sim 65$ and remains the larger component to late times. Eddy internal energy, like the 2-D internal energy, remains ~ 100 times smaller throughout the evolution.

It is apparent from the small internal energies in the 2-D and 3-D motion fields displayed in Figure 9 why the pressure-source term in the eddy kinetic energy equa-

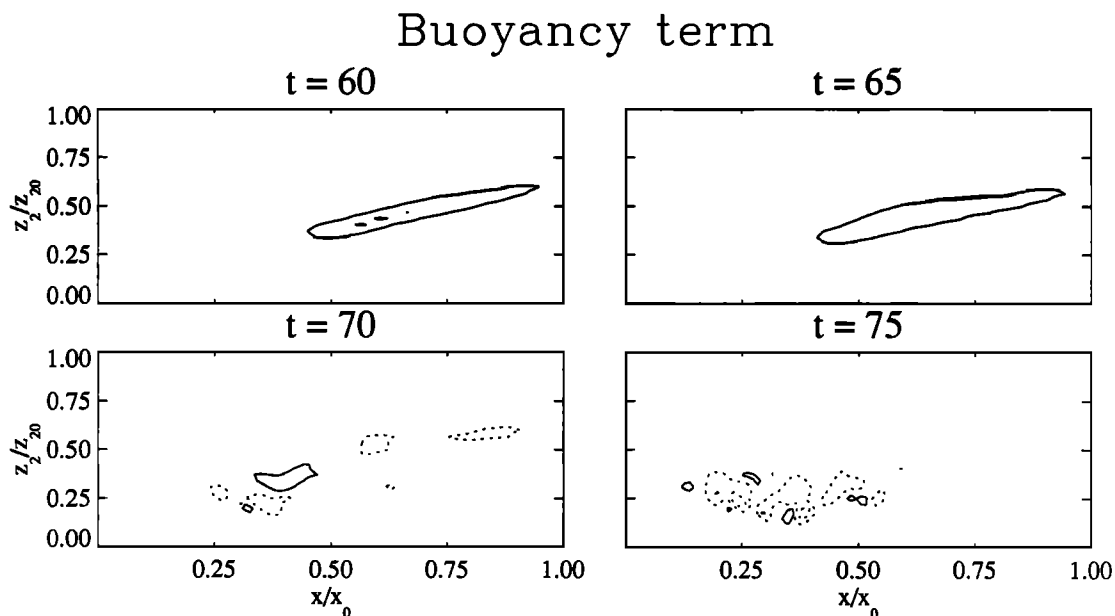


Figure 6. Buoyancy source/sink term of eddy kinetic energy as a function of (x, z) at $t = 60, 65, 70,$ and 75 . Contour intervals are 2.5×10^{-6} with positive (negative) solid (dashed) and those at $t = 60$ smaller by a factor of 5.

Vertical shear term

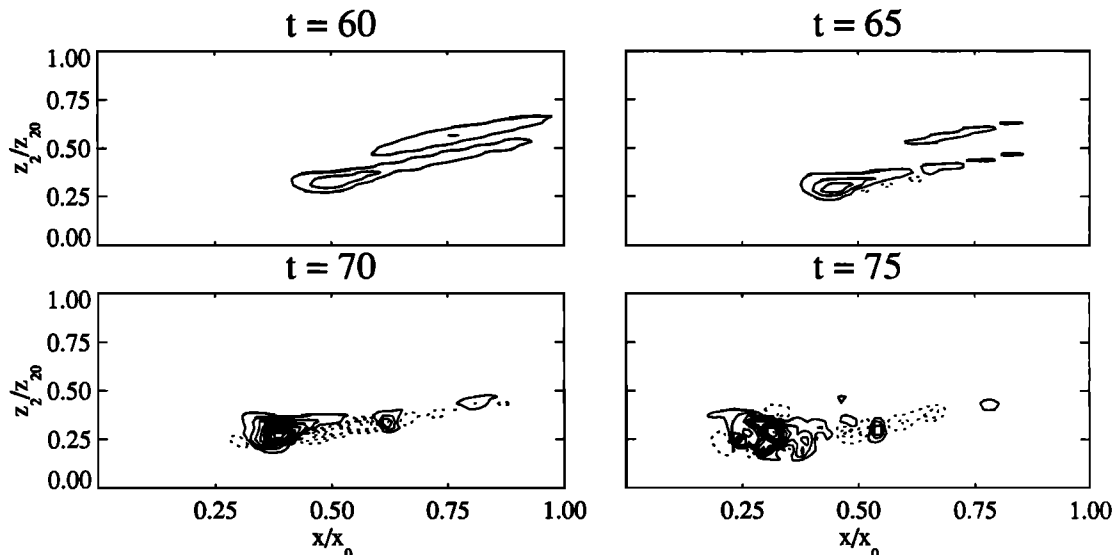


Figure 7. As in Figure 6, but for the vertical shear source/sink term.

tion was found to be negligible earlier in this section. These results also have implications for the importance of compressibility in our simulation. Specifically, the negligible role of pressure variations in the wave and eddy fields at large and small scales suggests that the dynamical effects of compressibility are not important in the evolution of a breaking wave and the transition to small-scale turbulence even for motions with relatively high intrinsic frequencies.

Instability Transports

Eddy transports of momentum and potential temperature are assessed in our model results by computing the

local and x -averaged values of $\langle u'w' \rangle$ and $\langle w'\theta' \rangle$. The local transports are displayed with (x, z) cross sections at $t = 60, 65, 70,$ and 75 in Figures 10 and 11. Profiles of the averaged eddy fluxes are shown in Figure 12. Eddy transports of energy are not displayed because they are found to be negligible relative to wave ($k_y = 0$) transports.

Momentum Fluxes

Eddy momentum fluxes arise largely in response to the local shear environment. In the absence of a mean shear, wave instability occurs near that phase of the wave motion in which the wave velocity is a maximum in the direction of propagation, suggesting that eddy

Horizontal shear term

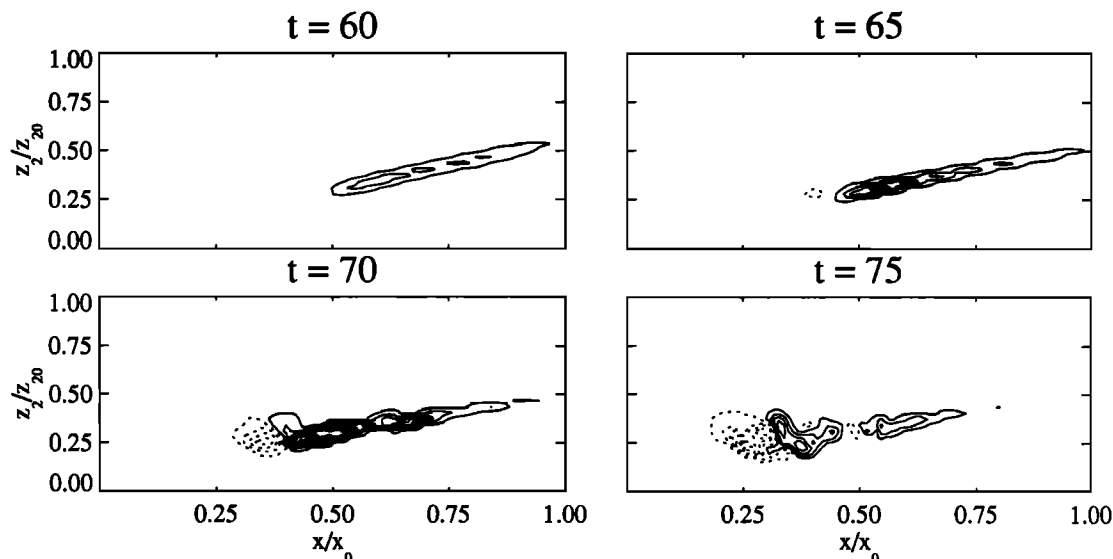
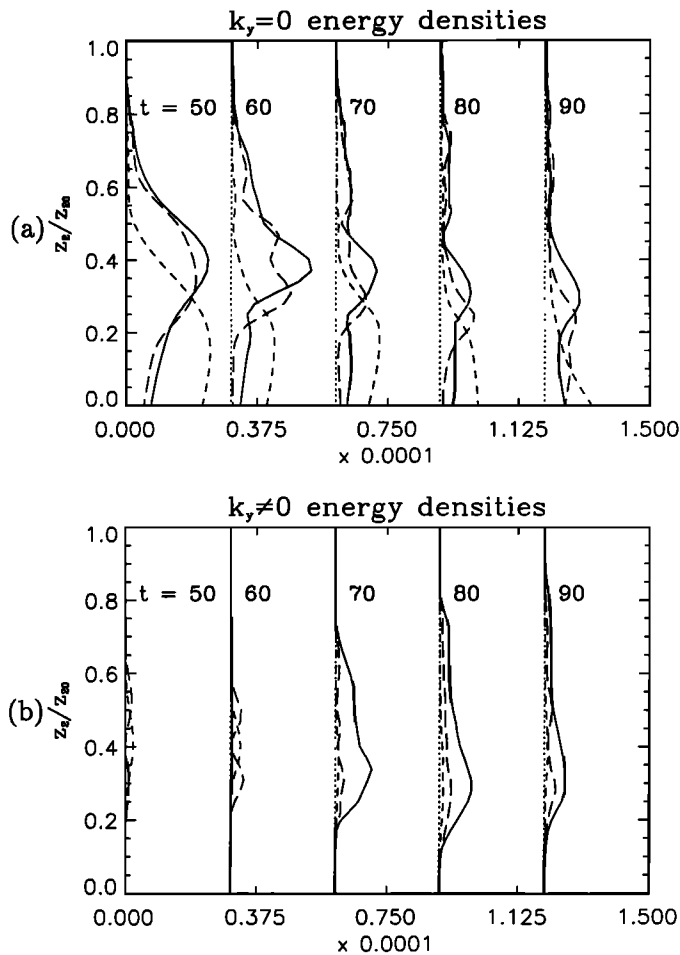


Figure 8. As in Figure 6, but for the horizontal shear source/sink term.



momentum fluxes should be small at this level. In our simulations, however, the eddy structures occur in the presence of significant wave and mean shears due to their large vertical extent (see Figure 9 of *Andreassen et al.* [this issue]). At early times, the dominant eddy momentum flux, $\langle u'w' \rangle$, is positive above and negative below the region of primary instability (upward and downward transports of positive x momentum), due to the negative and positive mean plus wave shears at these locations and times. Other components of the momentum flux, including $\langle u'v' \rangle$ and $\langle v'w' \rangle$, are also nonzero, due to asymmetries in the eddy structures, but are much smaller than $\langle u'w' \rangle$ and produce negligible changes in the mean motion field. The momentum flux profiles shown with solid curves in Figure 12 exhibit more simply the transition from transports due to vortex structures at early times to those due to dynamical instabilities of the local flow at later times.

Heat Fluxes

The eddy flux of potential temperature expressed as $\langle w'\theta' \rangle$ and shown at four times in Figure 11 is propor-

Figure 9. Profiles of kinetic (solid), potential (long dashed), and internal (short dashed) energy for the (a) $k_y = 0$ wave and (b) $k_y \neq 0$ eddy motions at $t = 50, 60, 70, 80,$ and 90 . The internal energy has been multiplied by 100 in each case for comparison and clearly represents a small fraction of the total energy.

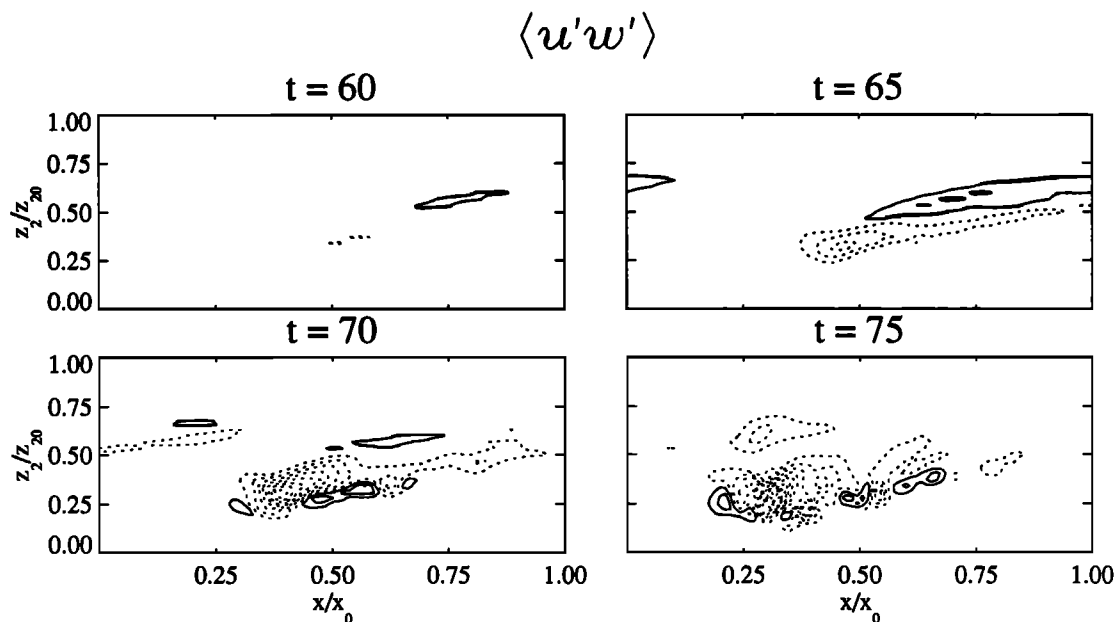


Figure 10. Eddy vertical transports of horizontal momentum per unit mass, $\langle u'w' \rangle$, in the (x, z) plane for $t = 60, 65, 70,$ and 75 . Positive (negative) contours are solid (dotted) and contour intervals are 2.5×10^{-4} (zero not shown). The momentum flux reverses sign initially due to the reversal of the large-scale shear across the unstable layer and is negative at later times due to dynamical instability at lower levels.

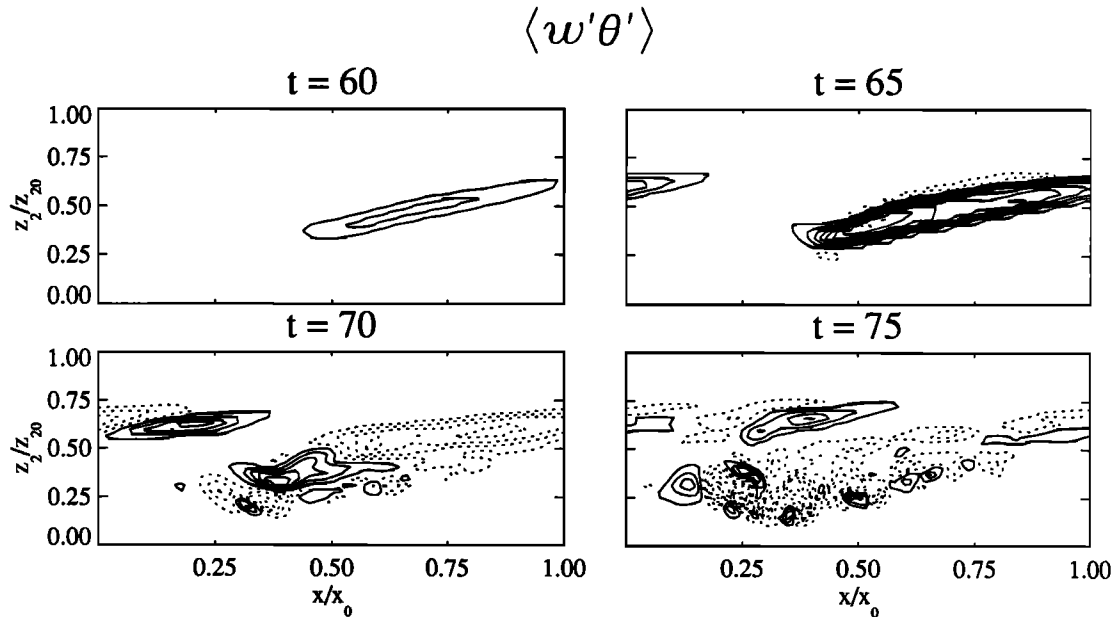


Figure 11. As in Figure 10, but for heat. Contour intervals are 1.6×10^{-4} . The initial positive heat flux acts to suppress the convective instability within the wave field, while at later times the heat flux is negative due to mixing of stably stratified fluid.

tional to the buoyancy source/sink term in the eddy kinetic energy equation. The contours display more structure in this case, however, because the three major source/sink terms were plotted on a common scale for easy comparison. As discussed above, the dominant flux of potential temperature by the eddy structures is upward at early times as a result of the inverted vertical gradient within the convectively unstable layer. This positive flux persists to later times at upper levels where the vortex structures and regions of convective instability evolve more slowly. Where the vortex structures have already contributed substantially to stabilization of the initially unstable layer, however, the flux reverses and achieves maximum negative values approximately half the positive maximum reached earlier (see the transition from $t = 65$ to 70 in Figure 11).

At lower levels of the flow where dynamical instability contributes to eddy kinetic energy at later times (see Figure 5 at $t > 70$ and Figures 5 and 9 of *Andreasen et al.* [this issue]), the flux of potential temperature is primarily negative due to eddy structures evolving in a stably stratified environment. This evolution is seen more clearly in the flux profiles (dashed curves) in Figure 12. The net flux of potential temperature is therefore highly sensitive to the stage of the wave field evolution and plays different roles at different times.

Summary and Conclusions

We have presented an analysis of the structure, evolution, and energetics of the instability responsible for the breaking and saturation of a large-amplitude gravity wave in three dimensions. The instability comprises pairs of counterrotating vortex structures analogous to the longitudinal rolls in sheared Rayleigh-Benard convection. Vortex structures are aligned along the plane of wave propagation (a horizontal wavenumber in the spanwise direction), are confined during their initial evolution to the convectively unstable regions within the wave field, and resemble closely the spanwise structures (with streamwise vorticity) observed to develop in unstable shear flows. Instability scales are selected based on the depth of the unstable layer and instability growth rates are large.

The major sources of instability (eddy) kinetic energy are buoyancy, primarily at early stages of the evolution, and eddy fluxes of momentum in regions of strong wave and mean shears, primarily at lower levels and later times. These eddy fluxes cause a rapid collapse of the unstable layers and restoration of near-adiabatic gradients within the wave field. Eddy energy flux (pressure

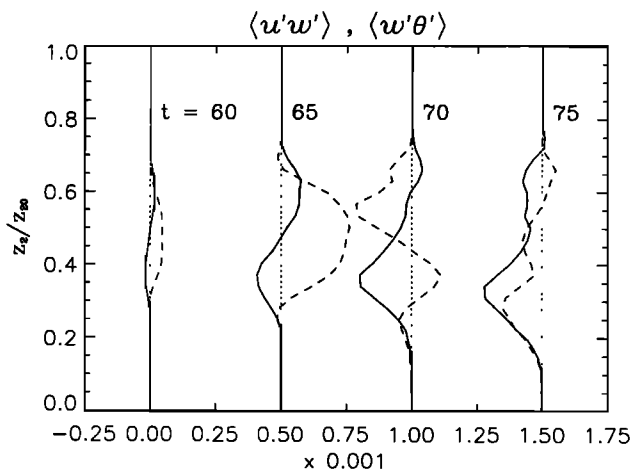


Figure 12. Profiles of eddy vertical momentum (solid) and heat (dashed) fluxes for $t = 60, 65, 70,$ and 75 .

work) and pressure-source terms, in contrast, are negligible relative to other contributions. Energy transfers occur initially within the wave field at $k_y = 0$ through systematic nonlinear interactions as wave amplitudes increase. Following the occurrence of convective instability, however, energy is transferred discontinuously to instability scales at transverse wavenumbers dictated by the depth of the instability. This transfer of energy to instability scales is reversed when eddy fluxes have largely stabilized the larger-scale flow.

The three-dimensional simulation of wave breaking examined here differs dramatically from that occurring in the parallel two-dimensional simulation discussed by *Andreassen et al.* [this issue]. This suggests that 3-D studies are necessary to describe adequately the instability structure accompanying wave breaking and its implications for wave amplitude limits, transports, spectral evolution, and turbulence generation and effects. 2-D models with these instability effects suitably parameterized may, nevertheless, describe wave effects and wave-mean flow interactions in more general applications at larger scales.

Acknowledgments. This research was supported by the Air Force Office of Scientific Research (AFSC) under grant F49620-92-J-0138, the SDIO/IST and managed by the Naval Research Laboratory under grant N00014-92-J-2005, and the Norwegian Defense Research Establishment. Extensive computer resources on the CRAY Y-MP at SINTEF in Trondheim, Norway were provided by the Norwegian Ministry of Science and Education. Additional resources on the CRAY Y-MP at NCAR in Boulder, Colorado were made available in association with National Science Foundation grant ATM91-18899. The Norwegian Research Council for Science and Humanities (NAVF) provided travel support for Ø. Andreassen during a stay at the University of Colorado in Boulder. The authors are also indebted to Colin Hines and one anonymous reviewer for valuable comments on the manuscript.

References

- Andreassen, Ø., I. Lie, and C. E. Wasberg, The spectral viscosity method applied to simulation of waves in a stratified atmosphere, *J. Comput. Phys.*, in press, 1993.
- Andreassen, Ø., C. E. Wasberg, D. C. Fritts, and J. R. Isler, Gravity wave breaking in two and three dimensions, 1. Model description and comparison of two-dimensional evolutions, *J. Geophys. Res.*, this issue.
- Bernal, L. P. and A. Roshko, Streamwise vortex structure in plane mixing layers, *J. Fluid Mech.*, 170, 499–525, 1986.
- Breidenthal, R., Structure in turbulent mixing layers and wakes using a chemical reaction, *J. Fluid Mech.*, 109, 1–24, 1981.
- Browand, F. K., and T. Troutt, A note on spanwise structure in the two-dimensional mixing layer, *J. Fluid Mech.*, 97, 771–781, 1980.
- Browand, F. K., and T. Troutt, The turbulent mixing layer: Geometry of large vortices, *J. Fluid Mech.*, 158, 489–509, 1985.
- Busse, F. H., and R. M. Clever, Instabilities of convection rolls in a fluid of moderate Prandtl number, *J. Fluid Mech.*, 91, 319–335, 1979.
- Clark, T. L., and R. D. Farley, Severe downslope windstorms in two and three spatial dimensions using anelastic interactive grid nesting: A possible mechanism for gustiness, *J. Atmos. Sci.*, 41, 329–350, 1984.
- Clever, R. M., and F. H. Busse, Three-dimensional convection in a horizontal fluid layer subjected to a constant shear, *J. Fluid Mech.*, 234, 511–527, 1992.
- Coy, L., D. C. Fritts, Gravity wave heat fluxes: A Lagrangian approach, *J. Atmos. Sci.*, 45, 1770–1780, 1988.
- Fritts, D. C., and T. J. Dunkerton, Fluxes of heat and constituents due to convectively unstable gravity waves, *J. Atmos. Sci.*, 42, 549–556, 1985.
- Gill, A. E., *Atmosphere-Ocean Dynamics*, Academic, San Diego, Calif., 1982.
- Isler, J. R., D. C. Fritts, and Ø. Andreassen, Gravity wave breaking in two and three dimensions, 3. Vortex breakdown and transition to isotropy, *J. Geophys. Res.*, this issue.
- Jimenez, J., A spanwise structure in the plane shear layer, *J. Fluid Mech.*, 132, 319–336, 1983.
- Klassen, G. P., and W. R. Peltier, The onset of turbulence in finite amplitude Kelvin-Helmholtz billows, *J. Fluid Mech.*, 34, 609–624, 1985.
- Lasheras, J. C., J. S. Cho, and T. Maxworthy, On the origin and evolution of streamwise vortical structures in a plane, free shear layer, *J. Fluid Mech.*, 172, 231–258, 1986.
- McIntyre, M. E., On dynamics and transport near the polar mesopause in summer, *J. Geophys. Res.*, 94, 14,617–14,628, 1989.
- Metcalfe, R. W., S. A. Orszag, M. E. Brachet, S. Menon, and J. J. Riley, Secondary instability of a temporally growing mixing layer, *J. Fluid Mech.*, 184, 207–243, 1987.
- Nagata, M., and F. H. Busse, Three-dimensional tertiary motions in a plane shear layer, *J. Fluid Mech.*, 135, 1–26, 1983.
- Pedlosky, J., *Geophysical Fluid Dynamics*, Springer-Verlag, New York, 1987.
- Pierrehumbert, R. T., and S. E. Widnall, The two- and three-dimensional instabilities of a spatially periodic shear layer, *J. Fluid Mech.*, 114, 59–82, 1982.
- Winters, K. B., and E. A. D'Asaro, 3D wave breaking near a critical level, *J. Fluid Mech.*, in press, 1993.
- Winters, K. B., and J. Riley, Instability of internal waves near a critical level, *Dyn. Atmos. Oceans*, 16, 249–278, 1992.

D. C. Fritts and J. R. Isler, Laboratory for Atmospheric and Space Physics and Department of Electrical and Computer Engineering, Campus Box 425, University of Colorado, Boulder, CO 80309.

Ø. Andreassen, Norwegian Defense Research Establishment, P. O. Box 25, N-2007, Kjeller, Norway.

(Received April 1, 1993; revised December 1, 1993; accepted December 1, 1993.)